NANO EXPRESS

Continuous and Localized Mn Implantation of ZnO

R. Sanz · J. Jensen · G. González-Díaz · O. Martínez ·
M. Vázquez · M. Hernández-Vélez

Abstract We present results derived from continuous and localized 35 keV $^{55}Mn^+$ ion implantations into ZnO. Localized implantations were carried out by using self-ordered alumina membranes as masks leading to ordered arrays of implanted volumes on the substrate surfaces. Defects and vacancies in the small implantation volumes of ZnO were generated due to the implantation processes besides the creation of new phases. Rapid thermal annealing was applied in the case of continuous implantation. The samples were characterized by HRSEM, GIXRD, Raman spectroscopy and RBS/C. Magnetic characterization of the samples pointed out appreciable differences among the samples obtained by the different implantation methods. This fact was mainly attributed to the different volume/surface ratios present in the implanted zones as well as to the increase of Mn atom concentrations along the grain frontiers in the nanostructured surfaces. The samples also showed a ferromagnetic transition phase at temperature value higher than room temperature.

Keywords Ion implantation · Nanoporous anodic alumina · Magnetic semiconductors · Magnetic properties · ZnO

R. Sanz (✉) · M. Vázquez · M. Hernández-Vélez
Instituto de Ciencia de Materiales de Madrid (CSIC), Sor Juana Inés de la Cruz, 3, 28049 Madrid, Spain
e-mail: ruy@icmm.csic.es

J. Jensen
Thin Film Physics Division, Department of Physics, Chemistry and Biology (IFM), Linköping University, 581 83 Linköping, Sweden

G. González-Díaz
Departamento de Física Aplicada III (Electricidad y Electrónica), Universidad Complutense de Madrid, Madrid, Spain

O. Martínez
Optronlab Group, Edificio I+D, Departamento de Física de la Materia Condensada, Universidad de Valladolid, Paseo de Belén, 1, 47011 Valladolid, Spain

M. Hernández-Vélez
Universidad Autónoma de Madrid, Carretera de Colmenar Viejo, Km. 15, Cantoblanco, 28049 Madrid, Spain

Introduction

Since the prediction of room temperature ferromagnetism in Mn:ZnO [1, 2] there has been great efforts to obtain this material, especially nanostructures, using a wide variety of strategies from the well-known material growth techniques to novel deposition and implantation methods [3–6]. The presence of ferromagnetism in this kind of materials was firstly claimed by Sharma et al. [7], while other authors founded spin glass, or simply non-magnetic behavior [3]. Previous works on Mn:ZnO pointed out different key factors determining the magnetic response of these novel materials, such as structural and composition changes, and atomic shared surfaces [8–10]. However, the existence of metastable phases [8] as a result of ion implantation processes can be a feasible explanation of such magnetic behavior. One of the most accepted hypotheses establishes that Mn atoms with different oxidation states sharing surfaces with intermediate O atoms are responsible of the observed magnetism. According to that, particularly in thin films, the shared surface between Mn atoms at the grain boundaries of different phases is a key condition to obtain ferromagnetic coupling. It is therefore reasonable to expect an enhanced ferromagnetic behavior in materials where the Mn atoms are arranged in a structure with a high surface to

volume ratio. Theoretically, this ferromagnetism is carrier mediated and thus the control of Mn atoms in sub-micro-metric confined volumes of ZnO matrixes is an important issue.

Experimental works on ion implantation of different atomic species into micrometric confined volumes [11] have shown that different diffusion and clustering properties of the implanted species may exist compared to continuum film implantation. The ion implantation processes usually give place to the generation of vacancies and point defects in crystalline matrixes, which strongly affect the carrier transport. In the particular case of Mn implanted ZnO, an anomalous creation of Zn interstitials has been studied 20 years ago [12] and, more recently, it has been reported that even non-doped ZnO nanostructures can show ferromagnetism [13] due to special arrangement of Zn and O atoms within ZnO crystalline structure confined into porous anodic alumina (PAA).

In this work first results following a new strategy of Mn:ZnO fabrication are presented. The objective is to elaborate a nanostructured array of implanted Mn:ZnO thin film using ZnO bulk single crystals as substrates, in order to study the effect of continuum versus localized ion implantation on the structural and magnetic properties. The Mn ion implantation into ZnO crystals surfaces is here performed by a continuum (i.e. conventional) method and, in addition, by using highly ordered self-assembly PAA membranes as implantation masks [14]. In the latter case, it is expected that the shared surface where Mn atoms have been implanted will increase and therefore an enhanced magnetic responses should be observed compared to the former implantation method.

Experimental

Small pieces of ZnO (wurzite) nominal single crystal (MTI Crystal Corp.) with polished m-plane surface orientation <100> and a density of 5.2 g cm^{-3} were used as substrates. Ion implantation was performed at normal incidence with 35 keV ^{55}Mn$^+$ ions to a total fluence of 4.2×10^{16} cm^{-2} and an average current density of 0.4 μA cm^{-2}. Simulation of the implantation profiles were carried out by the TRIM (version SRIM2006) [15] code, suggesting an essential Gaussian distribution, see Fig. 1a with a projected range of 20 nm and a straggling of 10 nm. The maximum peak concentration of Mn atoms is $\approx 22\%$. The lateral projected range and straggling were estimated to be 7 and 8 nm, respectively. After ion implantation, the so-called continuum implanted samples were annealed applying a rapid thermal annealing process (RTA) in O$_2$ atmosphere at 800 °C for 3 min.

Prior to the implantation process, some samples were covered with PAA membranes obtained by the well-known anodization processes reported elsewhere [16, 17]. The used PAA had a thickness of 2 μm, an average pore diameter of 265 nm and inter-pore spacings of 450 nm, see Fig. 1c. Consequently, the exposed areas of the substrates under the masks roughly correspond to 54% of the total area. The aspect ratio of the used mask allowed to performing the implantation without any alignment procedure [14, 18, 19]. According to the TRIM code, 35 keV ^{55}Mn ions are completely stopped by a 2 μm PAA membrane ($\rho = 2.3$ g cm^{-3} [17]), so substrate areas between the pores should not be exposed directly to the ion beam. In addition, no overlapping of implanted volumes seems possible due to the small lateral straggling compared to the distance between the pores, see Fig. 1b. Thus, the implanted volumes are predicted to have a disc shape distributed in a hexagonal centred array. Sample labels with a brief description are given in Table 1.

The samples were examined with high resolution scanning electron microscopy (HRSEM) using a Jeol Microscopy mod. JSM 6335F, micro-Raman spectroscopy with a HRLabRam spectrometer attached to a metallographic microscope. The excitation was done with a He–Ne laser line at 633 nm and grazing incidence (0.5°) X-ray diffraction (GIXRD) patterns were also received from Panalytical mod. X'Pert Pro, due to the special characteristics of M1 type of samples, the employed time in these measurements were 6 times longer compared to rest of samples types. In addition, random and channeling Rutherford backscattering spectrometry (RBS/C) was performed with 2 MeV ^{4}He$^+$ ions, backscattering angle 167°, in order to establish the experimental Mn distribution and damage profiles. The magnetic properties were determined in a superconductive quantum interference device (SQUID) before RBS measurements in order to not alter the magnetic response of samples. Magnetization as a function of temperature was measured under 1 kOe parallel to surface applied field from 4 to 300 K. Hysteresis loops were measured at the extreme temperature values.

Results and Discussion

Continuum Implanted Samples

θ–2θ XRD diffractograms of the virgin samples C0 showed only peaks associated to <100> ZnO (Fig. 2a). However, GIXRD of C0 presented diffraction peaks corresponding to the (110) ZnO crystalline planes in addition to the (100) (Fig. 2b). The (100) peak increased in intensity while the (110) peak decreased its intensity when increasing the incidence angle from 0.5 to 1°, suggesting a very thin ZnO

Fig. 1 **a** Simulation of Mn ion distribution depth. **b** Scheme of restricted implanted volumes. Surface HRSEM micrographs of **c** the original PAA mask and **d** the M1 sample after ion implantation and mask removal
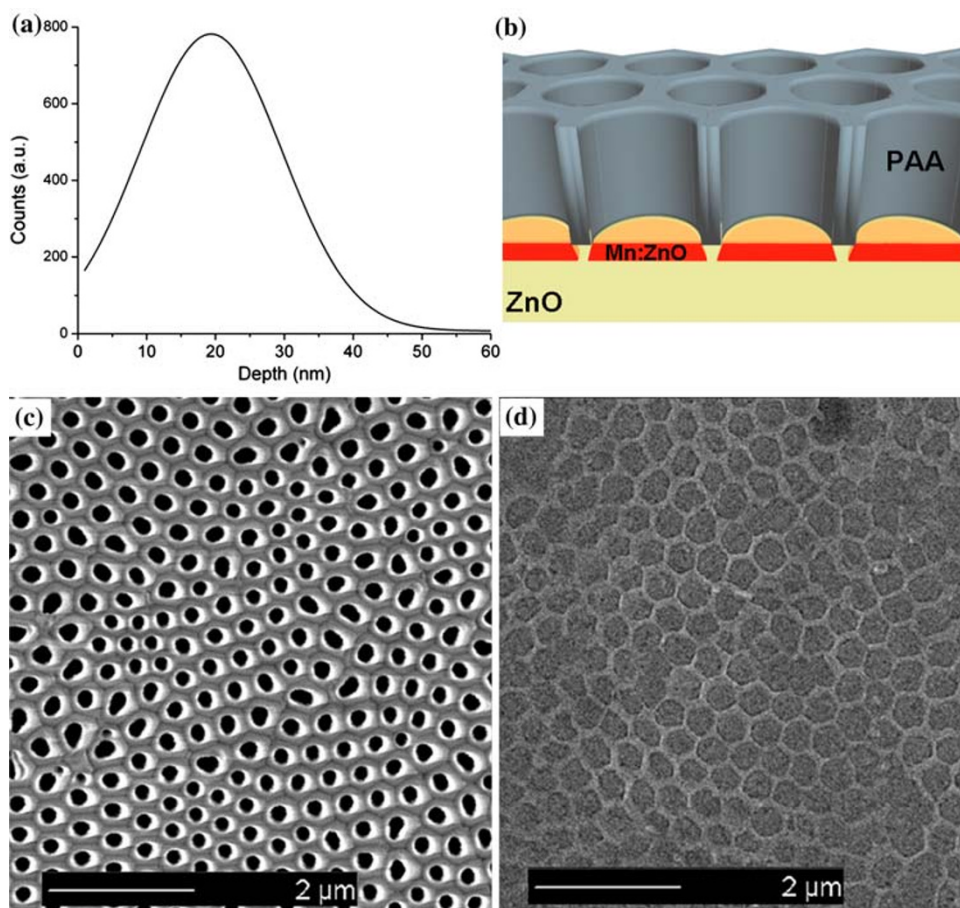

Table 1 Sample labels, obtained GIXRD results, crystalline phases, and estimated grain sizes of implanted samples

Sample type	Description	Main Bragg reflections	Mean grain size (nm)
C1	Continuum as-implanted	ZnO (110)	26.5
		$ZnMnO_3$ (511)	6.7
C2	Continuum implanted annealed	ZnO (103)	9.0
		ZnO (110)	22.0
		$ZnMnO_3$ (511)	5.7
		$ZnMnO_3$ (440)	16.6
M1	Masked as-implanted	ZnO (100)	12.7
		ZnO (110)	22.5
		$ZnMnO_3$ (511)	2.5

polycrystalline layer on top of the bulk ZnO single crystals. GIXRD diffractograms of the continuum implanted samples C1 and C2 showed differences in the structure compared to those received from C0 samples, see Fig. 2a. GIXRD spectra of C1 and C2 samples, Fig. 3a, showed broad peaks that can be associated to the overlapping of different crystalline phases of ZnO and $ZnMnO_3$ or simply to a contraction of ZnO structure due to the inclusion of Mn

atoms in the ZnO lattice. Therefore, it is rather difficult to unambiguously determine the structure using only this technique. The intensity of the peaks associated to the virgin ZnO samples is reduced for both C1 and C2 type samples. Nonetheless, a complete amorphization of ZnO is not expected due to its high amorphization threshold at room temperature [12]. Interestingly, in the C2 sample we observe a new peak, not seen in the original ZnO substrates, nor in C1. This peak is related to ZnO and $ZnMnO_3$ planes, revealing a polycrystalline structure.

Raman spectra of the C0 samples showed the typical vibrational modes of ZnO [20, 21] (see Fig. 4a). The registered spectra from as-implanted samples, C1 and M1, presented similar Raman bands in the 200–506 cm^{-1} range (Fig. 4b). They also exhibited a broadband ranging from 506 to 599 cm^{-1} which includes the 540 cm^{-1} peak ascribed to the ZnO 2LA mode [9]. Recently, this broadband has been detected in N$^+$- and P$^+$-implanted ZnO as well [22–24]. The C2 samples spectra did not display this broadband but showed similar features as C0 type (Fig. 4a) with only some differences in the intensity of the bands. This could be ascribed to the different crystalline orientations present in this sample after RTA treatment seen by GIXRD.
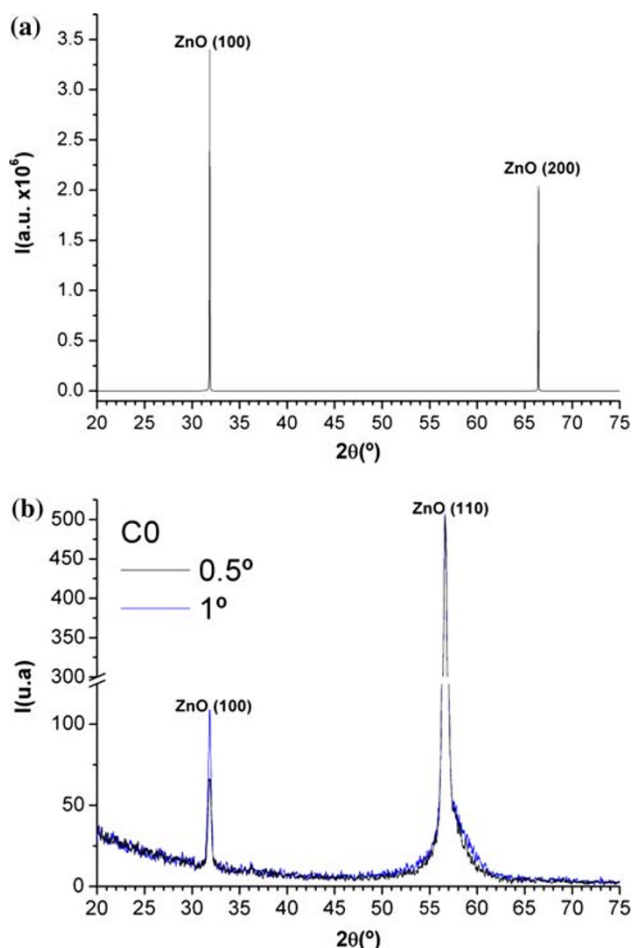
Fig. 2 a C0 XRD diffractogram in θ–2θ geometry. **b** C0 GIXRD diffractogram at 0.5 and 1°

Representative RBS channeling spectra of the Zn lattice are shown in Fig. 5 for samples belonging to C0, C1, and C2 types. Channeling measurements of C0 samples showed a $\chi_m = 9.3\%$. Channeling measurements of C1 samples revealed an average structural damage ($\chi_m = 58.8\%$) in the Zn lattice as far as 50 nm from the surface (channel 430-440). This damage peak did not reach the random level indicating that the sample is not fully amorphous in this region, confirming the GIXRD results. The Zn damage is followed by a peak at channel 417, which is due to the implanted Mn atoms. The maximum concentration of Mn is located at roughly 20 nm from the surface, in agreement with the TRIM simulation. Also, the estimated amount of implanted Mn from the spectra agrees, within the experimental error, with the simulations. The channeling spectra of C2 type samples exhibited a lower yield ($\chi_m = 41.2\%$) and a lesser broadening of the damaged zone signal near the surface than that observed for the C1 samples. The peak position related to the implanted Mn seems to remain at the same location as it was detected in sample C1. No broadening due to diffusion of the Mn profile is clear. Since

concentration profiles of both type of samples are quite similar, it is hard to elucidate if Mn atoms suffered some diffusion under the given annealing conditions [12]. The decrease of the channeling yields of C2 compared to C1 suggest that the original damaged ZnO crystalline lattice is partially recovered after the RTA process, once again, in agreement with the GIXRD results presented above.

For the C1 and C2 samples the measurements in RBS random geometry show that the Mn signal appears at about the same channel position as it was obtained in RBS channeling geometry. No significant modifications of the Mn atoms concentration profiles could be observed in both type of measurements. However, the yield of the Zn atoms decreased beyond channel 427 compared to the random level in the case of virgin samples C0. This fact indicates a diminution of the Zn atoms concentration from the surface to a maximum depth of approximately 80 nm. This decrease in the Zn atoms concentration is attributed to the increasing Mn atom concentration in that zone. Part of the Zn atoms are displaced to deeper locations, and it has previously been reported that Zn suffers anomalous displacement as interstitials defects [12].

Crystalline structure variations in the C1 samples compared to the C0 type due to the ion implantation were registered in the GIXRD and micro-Raman spectra, but no signal indicating Mn clustering was detected. The damages in the crystalline ordering can be summarized by the changes of the main crystallographic orientations detected in addition to the appearance of significant features that can be associated to the incipient formation of $ZnMnO_3$ or related crystalline phases. Although these phases were not identified from the micro-Raman analysis, the broadband displayed in the Raman spectra could reinforce the affirmation of the creation of a damaged zone with oxygen vacancies and/or Zn atom interstitials [25, 26]. The Raman spectra of the C2 samples have similar features as the C0 samples. For C2 samples the GIXRD spectra show an amorphous halo, which means that RTA induced only partial re-crystallization of the damaged zone followed by an increase of the grain size. The appearance of clear diffraction peaks in C2 spectra associated to ZnO and $ZnMnO_3$ phases, which were not detected in C0 and C1, can be attributed to the rearrangement of the Zn displaced atoms and the growing of texturized $ZnMnO_3$ as most probable compound. ZnO distorted signals were detected both in the GIXRD and micro-Raman spectra from C2 samples. The $ZnMnO_3$ XRD peaks were also detected in GIXRD spectra of these samples but this phase was not registered in micro-Raman spectrum obtained from C2 samples. This fact may be associated to $Zn_{1-x}Mn_xO$ unreacting metastable phase, which have been reported at temperatures lower than 750 °C [26], far from the detection limit of micro-Raman technique or a substitutional Mn:ZnO phase.

Fig. 3 a GIXRD representative diffractograms of C0, C1, and C2. **b** M1 sample (note the different scales). *Arrows* indicate ZnO orientation and crosses indicate ZnMnO$_3$ orientations
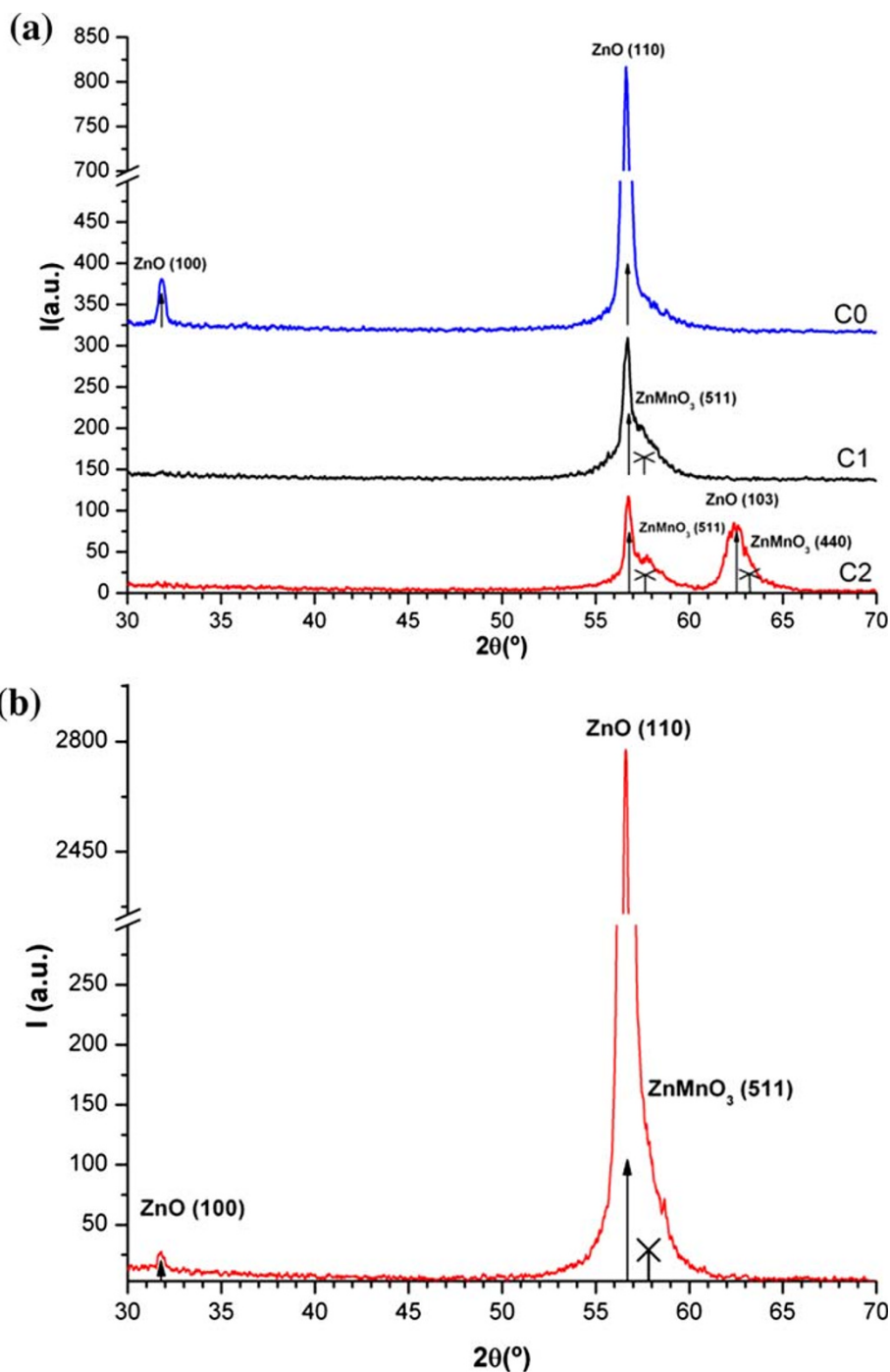
Masked Implanted Samples

HRSEM images of M1 samples displayed a noticeable ordered pattern of hexagonal symmetry at the surface, see Fig. 1d. This pattern is a consequence of the masking effect of the PAA during the ion implantation. In addition to sputtering of the substrate, the mask may also be subjected to some sputtering. There might even be some re-deposition of mask and substrate material. A simple TRIM estimation (assuming amorphous ZnO) gives a sputter depth of roughly 50 nm for the applied fluence, although this value is probably overestimated for a crystalline material. There is no clear evidence from the RBS results of C1 that there is such high sputtering depth. It should be noted that no signals from masks elements (Al and P) were detected with the employed techniques.

The GIXRD diffraction patterns of M1 samples presented similar features compared to that received from C1

Fig. 4 Micro-Raman spectra of the implanted samples: **a** C2 compared to C0 and **b** C1 compared to M1
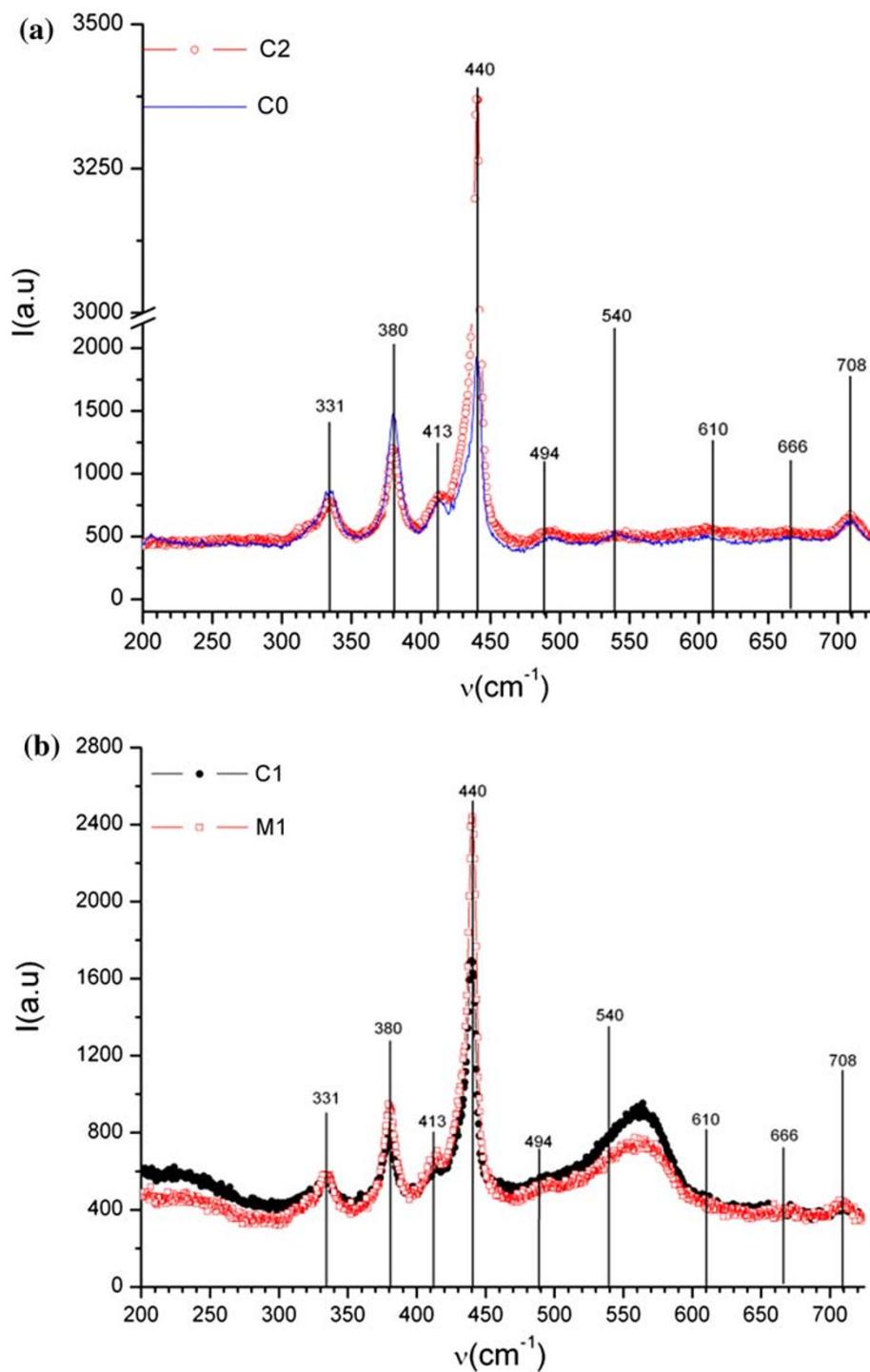
samples, Fig. 3b. Nonetheless, the M1 sample diffractogram clearly reflected the existence of a peak associated to <100> ZnO. The existence of this peak can be assigned to the non-implanted zones of ZnO substrate between the pores of PAA, which are affected by surrounding stresses from the implanted zones. The calculated grain size for <511> $ZnMnO_3$ in M1 samples was smaller than in C1 and C2. This effect may be ascribed to different diffusion

mechanisms in the localized implanted volumes, as previously observed by Sun et al. [11] following restricted Au implantation into TiO_2.

Raman spectra of the M1 samples also reflected similarities to those obtained for C1 samples. The observed broadband ranging from 506 to 599 cm^{-1} also point out the same implantation effects as in C1 type. However, the slightly lower intensity of this band points out a smaller
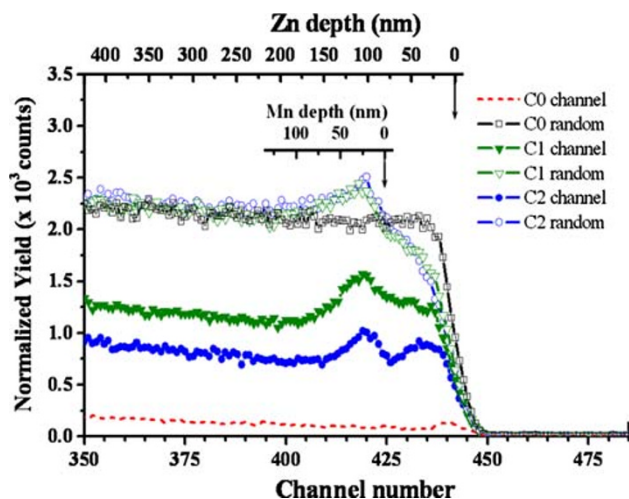
Fig. 5 Channeling RBS spectra of C0, C1, and C2 samples taken along the surface normal. The depth scales were obtained by using the surface energy approximation

damaged volume than that detected in C1 samples in accordance with the smaller volume affected by ion implantation. We have assumed that the induced damage volume and Mn atoms profile is similar to that in the continuum implanted sample, and the nanostructure of M1 samples is approximated by an array of discs with a diameter of 280 nm. We define the thickness of the discs as the combined width of the Mn distribution and the surrounding affected damaged volume, which from the RBS data can be around 50 nm.

Magnetic Characterization

Magnetic measurements showed hysteretic behaviors at 4 and 300 K for all implanted samples. Due to the large volume of the substrate (2 mm in thickness), compared to the thin implanted layer, the hysteresis loops exhibited a large linear diamagnetic signal, which is ascribed to the single crystalline ZnO substrate (data not shown). After removing these linear contributions from the raw data and normalize to the fluence of implanted Mn atoms (taking into account the different exposed surface in the M1 type samples), resultant characteristic hysteresis loops are shown in Fig. 6a and b. The coercive fields (H_c) and normalized remanence/saturation magnetization moment ratio (M_r/M_s) of samples were calculated (see Table 2). The hysteresis loops from C1 and C2 samples presented a softer magnetic behavior, i.e., lower coercive field than M1 sample. The increased coercive field in M1 can be associated to the effect of shape anisotropy, which is more intense in an array of implanted zones compared to a continuum implanted layer.

Magnetization values versus temperature between 4 and 300 K are shown in Fig. 6c, after subtraction of the linear

diamagnetic contribution from raw data and normalized to magnetization value at 4.2 K. In these curves a clear change at 275 K in all implanted samples can be observed. When the temperature is increased, the magnetization values suffer an abrupt decreasing at 275 K, which can be associated to magnetic phase changes. These changes become much clearer from the derivate of M(T) plotted in Fig. 5d for all samples. The most noticeable dips are seen in the M1 and C2 samples at 275 K. The observation of hysteresis loop for this temperature indicates the presence of a common ferromagnetic phase in all samples having a Curie temperature (T_C) higher than 300 K.

The presence of a hysteretic behavior, at 4 and 300 K, can be associated to ferromagnetism, although alternative cooperative magnetic interactions can be argued [27], such as ferrimagnetism or antiferromagnetism in coexistence with ferromagnetism. The observed magnetic response can be explained in terms of multiphase system where the existence and interaction of diverse compounds and metastable phases are given as it was indicated by the structural characterization.

A starting point for this explanation would be to identify a phase with a T_C at 275 K and to rule out those for which their T_C does not fit with 275 K. The explanation of the observed magnetic response might be ascribed to diverse manganese oxides [28], e.g., MnO, Mn_2O_3 and MnO_2, which are well known to be antiferromagnetic below the Néel temperature of 116, 100 and 84 K, respectively, and bulk Mn_3O_4 exhibiting ferromagnetism with $T_C = 42$ K. Magnetic behavior of several transition metal-ZnO spinels have recently been reported [29], with T_C lower than 275 K being the temperature at which a magnetic phase change occurs in our samples. However, $ZnMnO_3$ has a T_C higher than 300 K [29], so the formation of this phase explains the hysteretic response at 300 K observed for all samples and its relative abundance might explain the different M_s values at 300 K, for the different sample.

The observed magnetic ordering at temperatures lower than 275 K can be explained by assuming that part of the Mn atoms form non-ferromagnetic compounds [29] but with different magnetic susceptibility from ZnO, and that the other part of Mn atoms participate in (1) a short range indirect exchange and (2) a double exchange mechanisms [27]. In the first case, the magnetic interaction results in antiferro- or ferromagnetic ordering, whereas in the second case it results in ferromagnetic coupling. These mechanisms have been reported for systems where there are highly shared surfaces, e.g. thin multilayers [8–10] and the Mn atoms present different oxidation states. Our systems have similar characteristics to those mentioned above. There is a high ratio between Mn atoms situated on shared surfaces, at grain boundaries and atoms inside those grains of polycrystalline implanted volumes. This ratio is higher
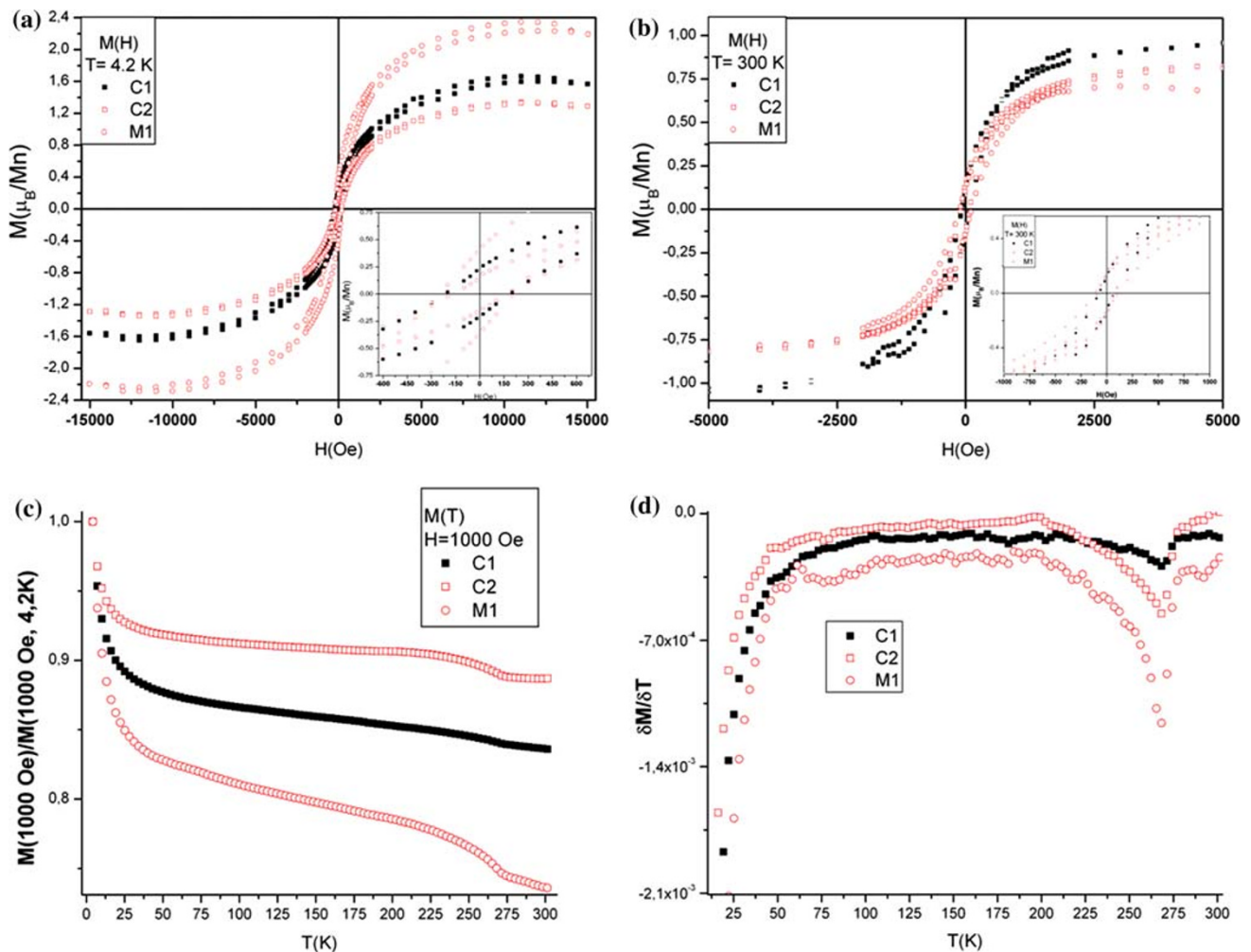
Fig. 6 Magnetic measurements of the C1, C2 and M1 samples. **a** 4 K and **b** 300 K. The magnetization has been normalized to the number of implanted Mn atom. **c** M(T) as function of temperature measured at 1000 Oe and normalized to M_s (4 K, 1000 Oe) and **d** its derivate

Table 2 Magnetic properties of the different samples measured at 4 K and 300 K

	C1		C2		M1	
T (K)	4.2	300	4.2	300	4.2	300
H_c (Oe)	123	77	109	75	269	121
M_r/M_s	0.22	0.11	0.15	0.15	0.27	0.11
M_s (μ_B/Mn)	1.6	1.15	1.3	0.8	2.2	0.7

H_c is the mean coercive field, M_r is the remance field, and M_s is the saturation magnetic moment. M stands for magnetization. M_r and M_s have been normalized to the total amount of implanted Mn atoms. Note the number of implanted atoms in M1 is different from the other cases

in masked implanted samples than in not masked ones. The high M_s per implanted Mn atom fits well with that obtained by Norberg et al. [5] for thin nanocrystalline films. This fact reinforce the idea referred to that the magnetism

appearing in all theses structures is originated by Mn atoms with different oxidation states situated at the grain boundaries of different phases.

On the other hand, the confirmed partial recovering of the crystalline ordering in the annealed sample is also responsible for a local arrangement of ions and therefore of different magnetic responses. The existence of defects and vacancies are key factors for the magnetic behavior of doped ZnO [3, 30]. In our case, there are no definitive and clear evidences of substitutional Mn; however, the existence of O vacancies and Zn defects, the last ones detected by RBS, induced by the ion implantation process in ZnO, plays an important role. For example, the O vacancies favor antiferromagnetism and Zn defects contribute to ferromagnetism [31], but also these vacancies and defects change the magnetic permeability from original ZnO. M1 and C1 samples reflected more damaged crystalline structure than C2 type. Thus, it can be assumed that in those samples, the enhanced magnetic response per Mn atom is

highly influenced by the partial loss of crystalline order, the existence of associated defects and also by participation of more Mn atoms on the grain boundaries compared to C2 sample. Inclusive, the even higher participation of Mn atoms located at grain boundaries in M1 samples makes the magnetic response in this sample higher than in C1 sample.

Conclusions

Manganese ions of 35 keV have been successfully implanted into ZnO. The ion implantations were carried out, both in a conventional way (yielding a continuous thin layer), and locally through the pores of a PAA. In the latter case, a nanostructured surface with surface/volume ratio higher than that achieved in the continuous implanted samples was obtained improving the magnetic response.

Differences in the structure after implantation and RTA were detected and associated to preferential crystalline planes and changes in grain sizes at the nanometric scale. RTA in O_2 atmosphere partially recovered the crystalline order, but did not indicate an appreciable diffusion of Mn atoms in the ZnO matrix. Structural results indicated a probable recrystallization processes and the existence of metastable phases even after RTA. The analyzed magnetic responses suggest cooperative interactions between these phases which increase the values of the saturation magnetization. The activation temperature of the detected magnetic phases at 275 K does not correspond to those previously reported for Mn and Zn–Mn oxides, in accordance with the observed structural results. The origin of room temperature ferromagnetism has been associated to $ZnMnO_3$ as the most probable compound.

The higher values of H_c in the locally implanted sample were ascribed to shape anisotropy. The increasing numbers of Mn atoms participating in the magnetic interaction due to the increased shared surfaces at grain boundaries and the generated defects by the ion implantation improve the quality of the magnetic response in masked sample compared to the continuum implanted one. The techniques reported here may be useful for designing new fabrication methods for nanostructured devices or to induce high concentration levels of impurities and defects in confined volumes.

References

1. T. Dietl, H. Ohno, F. Matsukura, J. Cibert, D. Ferrand, Science **287**, 1019 (2000). doi:10.1126/science.287.5455.1019
2. K. Sato, H. Katayama-Yoshida, Jpn. J. Appl. Phys. **40**(Part 2), L334 (2001). doi:10.1143/JJAP.40.L334
3. C. Jagadish, S. Pearton (eds.), *Zinc Oxide Bulk, Thin Films and Nanostructures: Processing, Properties and Applications* (Elsvier, Amsterdam, 2006)
4. J.B. Wang, G.J. Huang, X.L. Zhong, L.Z. Sun, Y.C. Zhou, E.H. Liu, Appl. Phys. Lett. **88**, 252502 (2006). doi:10.1063/1.2208564
5. N.S. Norberg, K.R. Kittilstved, J.E. Amonette, R.K. Kukkadapu, D.A. Schwartz, D.R. Gamelin, J. Am. Chem. Soc. **126**, 9387 (2004). doi:10.1021/ja048427j
6. W.B. Mia, H.L. Bai, H. Liu, C.Q. Sun, J. Appl. Phys. **101**, 023904 (2007)
7. V.K. Sharma, G.D. Varmaa, J. Appl. Phys. **102**, 056105 (2007). doi:10.1063/1.2778283
8. C. Darshan, C. Kundaliya, S.B. Ogale, S.E. Lofland, S. Dhar, C.J. Metting, S.R. Shinde, Z. Ma, B. Varughese, K.V. Ramanujachary, L. Salamanca-Riba, T. Venkatesan, Nat. Mater. **3**, 709 (2005)
9. M.A. García, M.L. Ruiz-González, A. Quesada, J.L. Costa-Krämer, J.F. Fernández, S.J. Khatib, A. Wennberg, A.C. Caballero, M.S. Martín-González, M. Villegas, F. Briones, J.M. González-Calbet, A. Hernando, Phys. Rev. Lett. **94**, 217206 (2005). doi:10.1103/PhysRevLett.94.217206
10. E. Céspedes, J. Garcia-López, M. García-Hernández, A. de Andrés, C. Prieto, J. Appl. Phys. **102**, 033907 (2007). doi:10.1063/1.2764207
11. K. Sun, S. Zhu, R. Fromknecht, G. Linker, L.M. Wang, Mater. Lett. **58**, 547 (2004). doi:10.1016/S0167-577X(03)00559-7
12. E. Sonder, R.A. Zuhr, R.E. Valiga, J. Appl. Phys. **64**, 1140 (1988). doi:10.1063/1.341875
13. J.B. Yi, H. Pan, J.Y. Lin, J. Ding, Y.P. Feng, S. Thongmee, T. Liu, H. Gong, L. Wang, Adv. Mater. **20**, 1170 (2008)
14. M. Nakamura, S. Nigo, N. Kishimoto, Trans. Mater. Res. Soc. Jpn. **33**, 1101 (2008)
15. www.srim.org. Accessed 30 Apr 2009
16. R. Sanz, A. Johansson, M. Skupinski, J. Jensen, G. Possnert, M. Boman, M. Vazquez, K. Hjort, Nano Lett. **6**, 1065 (2006). doi:10.1021/nl0602185
17. M. Hernández-Vélez, Thin Solid Films **495**, 51 (2006). doi:10.1016/j.tsf.2005.08.331
18. R. Sanz, J. Jensen, A. Johansson, M. Skupinski, G. Possnert, M. Boman, M. Hernandez-Vélez, M. Vazquez, K. Hjort, Nanotechnology **18**, 305303 (2007). doi:10.1088/0957-4484/18/30/305303
19. S.W. Shin, S.G. Lee, J. Lee, C.N. Whang, J.-H. Lee, I.-H. Choi, T.G. Kim, J.H. Song, Nanotechnology **16**, 1396 (2005). doi:10.1088/0957-4484/16/8/070
20. J.M. Calleja, M. Cardona, Phys. Rev. B **16**, 3753 (1997). doi:10.1103/PhysRevB.16.3753
21. R. Cuscó, E. Alarcón-Lladó, J. Ibáñez, L. Artús, J. Jiménez, B. Wang, M.J. Callahan, Phys. Rev. B **75**, 165202 (2007). doi:10.1103/PhysRevB.75.165202
22. L. Artús, R. Cuscó, E. Alarcón-Lladó, G. González-Díaz, I. Mártil, J. Jiménez, B. Wang, M.J. Callahan, Appl. Phys. Lett. **90**, 181911 (2007). doi:10.1063/1.2734474
23. Z.Q. Chen, A. Kawasuso, Y. Xu, H. Naramoto, X.L. Yuan, T. Sekiguchi, R. Suzuki, T. Ohdaira, J. Appl. Phys. **97**, 013528 (2005). doi:10.1063/1.1821636
24. J. Yu, H. Xing, Q. Zhao, H. Mao, Y. Shen, J. Wang, Z. Lai, Z. Zhu, Solid State Commun. **138**, 502 (2006). doi:10.1016/j.ssc.2006.04.019

25. S. Venkataraj, N. Ohashi, I. Sakaguchi, Y. Adachi, T. Ohgaki, H. Ryoken, H. Haneda, J. Appl. Phys. **102**, 014905 (2007). doi:10.1063/1.2752123

26. F. Buciuman, F. Patcas, R. Craciun, R.T. Zahn Dietrich, Phys. Chem. Chem. Phys. **1**, 185 (1999). doi:10.1039/a807821a

27. R.C. O'Handley, *Modern Magnetic Materials: Principles and Applications* (Wiley, New York, 2000)

28. E.P. Wohlfarth, *Ferromagnetic Materials: A Handbook on the Properties of Magnetically Ordered Substances*, vol 3 (North-Holland Physics Publishing, Amsterdam, 1982)

29. J. Blasco, J. García, J. Solid State Chem. **179**, 2199 (2006). doi:10.1016/j.jssc.2006.04.026

30. S. Zhou et al., J. Phys. D: Appl. Phys. **41**, 105011 (2008). doi:10.1088/0022-3727/41/10/105011

31. A.L. Rosa, R.J. Ahuja, J. Phys. Condens. Matter **19**, 386232 (2007). doi:10.1088/0953-8984/19/38/386232